Icarus 317 (2019) 148–157

Contents lists available at ScienceDirect

Icarus

journal homepage: www.elsevier.com/locate/icarus

Age of martian air: Time scales for martian atmospheric transport

D.W. Waugh[a,*], A.D. Toigo[b], S.D. Guzewich[c]

[a] Department of Earth and Planetary Science, Johns Hopkins University Baltimore, 3400N Charles St, Baltimore, MD, USA
[b] Johns Hopkins University Applied Physics Laboratory, Laurel, MD, USA
[c] NASA Goddard Space Flight Center, Greenbelt, MD, USA

ABSTRACT

The mean time since air in the Martian atmosphere was in the low-latitude boundary layer is examined using simulations of an idealized "mean age" tracer with the MarsWRF general circulation model. The spatial distribution and seasonality of the mean age in low- and mid-latitudes broadly follow contours of the mean meridional circulation, with the mean age increasing from 0 at the surface to a maximum of 60–100 sols in the upper atmosphere. Substantially older mean ages (exceeding 300 sols) are found in polar regions, with oldest ages in the lower atmosphere (10–100 Pa), above a near-surface layer with very young ages (around 20 sols). The annual maximum ages occur around the equinoxes, and the age in the polar lower atmosphere decreases during the autumn to winter transition. This autumn-winter decrease in age occurs because of mixing of polar and mid-latitude air when the polar vortex exhibits an annulus of high potential vorticity (PV) with a local minimum near the pole. There is no autumn-winter decrease and old ages persist throughout autumn and winter in simulations with CO_2 phase changes disabled, and thus no latent heating, where there is a monopolar vortex (i.e., a monotonic increase in PV from equator to pole) forms. The altitudinal and seasonal variations in the mean age indicates similar variations in the transport of dust into polar regions and the mixing of polar air (with, e.g., low water vapor and high ozone concentrations during winter) into mid-latitudes.

1. Introduction

Transport plays an important role in controlling the atmospheric composition of Mars and other planets. Particularly important for the global climate of Mars are the distributions of dust and ice (H_2O and CO_2) aerosols, and it is important to understand and quantify the transport from, between, and to different source and sink regions and how the transport varies with changes in global and synoptic dynamics (e.g., Clancy et al., 1996; Smith, 2002a,b; Bertaux et al., 2005). Unfortunately, limited quantitative information can be extracted from existing spacecraft observations alone. Constraints on some aspects of the transport have been obtained from observations, e.g., of argon (e.g., Sprague et al., 2007, Lian et al., 2012), ozone (Montmessin and Lefevre, 2013), water vapor (Smith, 2002a,b), and dust (Newman et al., 2002), either from observations alone or in combination with general circulation model simulations.

While simulations of real, observable tracers have the advantage that the results can be compared with observations, it is difficult to extract quantitative transport information as the tracer distributions depend not only on transport but also on (often uncertain) sources and loss processes (e.g., chemical reactions, phase changes, sedimentation). An alternative approach is to use general circulation models to simulate the distribution of idealized tracers which are designed to quantify aspects of the transport. This is common in studies of Earth's atmosphere, and a variety of idealized tracers have been simulated to quantify different aspects of transport (e.g., Plumb and Mahlman, 1987; Hall and Plumb, 1994; Orbe et al., 2013). However, this not a common approach in studies of the Martian atmosphere. One exception is Barnes et al. (1996), who estimated eddy mixing coefficients and "ventilation" timescales in a Mars general circulation model. They found that the eddy mixing and ventilation time scales varied with season and with dust loading, with faster ventilation during dusty solstice conditions.

In this paper we present another such study. Specifically, we use the MarsWRF general circulation model to calculate the mean time since air in the Martian atmosphere was in the low- to mid-latitude boundary layer. Similar calculations of the "mean age" (or age of air) are common in studies of transport in Earth's stratosphere (e.g., Hall and Plumb, 1994; Waugh and Hall, 2002) and, more recently, in Earth's troposphere (Waugh et al., 2013; Orbe et al., 2017; Krol et al 2017). The mean transit time to a location is a fundamental aspect of the transport, and has been used in studies of Earth's atmosphere to quantify the propagation of changes in concentration of constituents (e.g. anthropogenic pollutants) through the atmosphere, and to identify partial barriers to transport (e.g. the edge of stratospheric polar vortices or edges of Hadley Cells). Understanding the variations in the mean age of air in the Martian atmosphere has the potential to help in understanding the distribution of dust, water vapor, and other trace gases on

* Corresponding author.
E-mail addresses: Waugh@jhu.edu (D.W. Waugh), anthony.toigo@jhuapl.edu (A.D. Toigo), scott.d.guzewich@nasa.gov (S.D. Guzewich).

https://doi.org/10.1016/j.icarus.2018.08.002
Received 3 January 2018; Received in revised form 16 May 2018; Accepted 1 August 2018
Available online 02 August 2018
0019-1035/

Mars.

The model and tracer simulations are described in the next section. The results from the standard simulation are presented in Section 3, while results from additional simulations to test sensitivity of age distribution to CO_2 microphysics, additional dust loading, or source region extent are described in Section 4. Concluding remarks are in the final section.

2. Methods

2.1. Model and simulations

Numerical experiments are performed using the MarsWRF general circulation model (Toigo et al., 2012). The simulations use the same MarsWRF configuration as in Toigo et al. (2017) except for the inclusion of a mean age tracer (see below), and only a brief description is given here. The MarsWRF simulations were conducted at $2^\circ \times 2^\circ$ spatial resolution, with 52 vertical levels, and with a transverse map projection grid that displaces the mathematical pole of the projection to two (antipodal) locations on the equator so as to preserve more accurate representation of the geographic poles. The model includes a parameterization scheme in which condensation and sublimation of CO_2, and subsequent exchange of latent heat, occurs when temperatures fall below or rise above the condensation point (based on local temperature and pressure conditions). When CO_2 condensation occurs in the atmosphere, it is deposited directly on the surface, and the column mass (and hence atmospheric pressure at the surface) is updated and redistributed vertically to account for CO_2 loss or gain in the atmosphere (see Richardson et al. (2007) for details).

We examine the transport in the "standard" MarsWRF simulations from Toigo et al. (2017), as well as the "no-CO_2-latent-heating" and "additional dust" simulations also discussed there to test the sensitivity of transport to alternate forcings. The "standard" simulation employs the previously mentioned scheme for CO_2 phase changes and the prescribed dust distribution is based on the "MGS Scenario" as described in Lewis et al. (1999) and Montmessin et al. (2004). The "no-CO_2-latent-heating" simulation uses the same dust distribution but the CO_2 microphysics parameterization is disabled such that there are neither phase changes nor latent heat exchange. The "additional dust" simulation includes the parameterization for condensation and sublimation of CO_2, but a seasonal peak (near perihelion and southern summer solstice) of global-average column-integrated dust opacity twice that of the standard "MGS Scenario" distribution. This simulation also corresponds to the "high dust" simulation of Guzewich et al. (2016). All simulations were run for 3 Mars years with only the third year of results shown. The standard simulation was run for an additional two years to examine the interannual variability.

2.2. Mean age tracer

To quantify the transport from the surface to different regions in the atmosphere an idealized "mean age" tracer that yields the mean time since air was at surface "source" region is included in the simulations. Similar mean age (or age of air) tracers are commonly used in studies of transport in Earth's stratosphere and troposphere (e.g., Waugh and Hall, 2002; Waugh et al., 2013; Orbe et al., 2017). The governing equation for this idealized mean age tracer $\Gamma(\mathbf{x}, t)$ is

$$\frac{\partial \Gamma}{\partial t} + (L) = 1$$

where L is the linear transport operator, including advective and diffusive transport (Haine and Hall, 2002). The boundary condition is $\Gamma(\Omega,t) = 0$ where Ω is the "source" region, and $\Gamma(\mathbf{x},0) = 0$ initially. In other words, the tracer is initially set to a value of zero throughout the atmosphere, is held to be zero over Ω, and subject to a constant aging of 1 sol per sol (where one sol is one Martian "day") in the rest of the atmosphere. Here Ω is taken as the lowest 10 km of the atmosphere between 45°S to 45°N, to roughly represent the low-to-mid-latitude boundary layer region of the Martian atmosphere, and the idealized mean age tracer yields the mean transport time from this region. (From here on, we will refer to the idealized mean age tracer as the "mean age", or just "age", for convenience and simplicity.)

In addition to the two sensitivity simulations mentioned above, two further simulations to test the sensitivity to the size of the source region Ω were also performed. These two simulations use the same set up as the standard simulation, but the tracer source region is altered to have either a lower height (5 km) or a narrower extent (30°S–30°N); these simulations are referred to as the "shallow source" and "narrow source" simulations, respectively.

The evolution of the mean age tracer is simulated using the standard transport scheme in MarsWRF, which is identical to that used in the original terrestrial WRF model (Skamarock et al., 2008; Skamarock and Klemp, 2008). There is no sub-grid-scale convective mixing nor explicit diffusion, so that the model simulates the conservative and passive transport of the mean age tracer only by the explicitly-resolved winds. Furthermore, as the mean age tracer is defined to yield the mean transit time, rather than the mass or number concentration of an atmospheric constituent, there is no rescaling of the concentration of the tracer when mass is added to or removed from the atmosphere through sublimation or deposition in the polar regions.

3. Standard simulation

3.1. Global distribution

We first consider the spatial distribution of the zonal- mean age Γ, and how it varies seasonally. Fig. 1 shows the latitude-pressure variation of the zonal-mean Γ, at each equinox and solstice. As expected, there is a general increase in Γ with distance from the source region, both with increasing height and latitude. At low- and mid-latitudes Γ increases from zero at the surface to 60–90 sols at 1 Pa, and above the surface layer there is a large increase from low- to high-latitudes (e.g., at 50 Pa, Γ increases from less than 20 sols at the equator to values exceeding 200 sols in polar regions).

The general structure of the Γ distribution shown in Fig. 1 can be broadly explained in terms of the mean meridional circulation (red contours) and Hadley cell circulations. The youngest ages are within the Hadley cells, and the regions of youngest age generally follow the seasonal changes of the Hadley cell circulations. At the solstices there is a single nearly pole-to-pole Hadley cell from summer to winter hemisphere, which results in younger air in summer than in winter mid-latitudes in the upper atmosphere (10–1 Pa). In contrast, at the equinoxes there are weak Hadley cells in each hemisphere and these transport air up from the near-surface in equatorial regions and towards each pole at higher altitudes, and as a result in the upper atmosphere there are weak meridional age gradients at all latitudes.

3.2. Polar regions

Unlike at lower latitudes, the oldest air in polar regions is in the lower atmosphere (10–100 Pa) and not the upper atmosphere. The youngest ages at the poles are still near the surface and age increases with height in lower atmosphere, but then decreases from lower-middle atmosphere to the upper atmosphere. Thus, in polar regions Γ does not increase monotonically with altitude. Furthermore, Γ in the polar lower atmosphere (100–10 Pa) is generally much older than that anywhere in the low- and mid-latitudes, i.e., the polar age can exceed 250 sols, greater than what is seen at any altitude in the low- and mid-latitudes.

There is also much larger seasonality of Γ in the polar regions than at lower latitudes, with the annual variation of Γ in some regions over 200 sols (e.g., Γ at 100 Pa varies from around 50 sols to over 250 sols). This seasonality in polar age is shown clearly in Fig. 2, which shows the

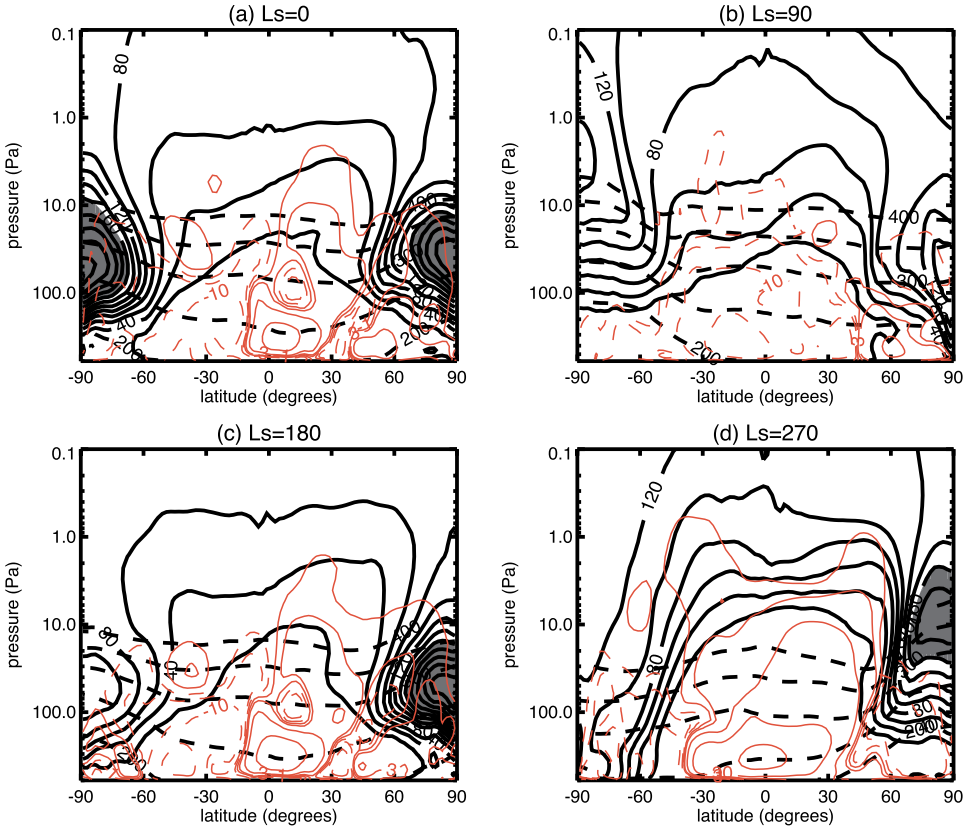

Fig. 1. Latitude-pressure variation of zonal-mean Γ for Ls = (a) 0°, (b) 90°, (c) 180°, and (d) 270°, for the "standard" simulation. Contours every 20 sols, with values larger than 160 sols shaded. Thin red contours show the mean meridional circulation (contours at [−100, −30, −10, −3, −1, 1, 3, 10, 30, 100] x 10^8 m^2/s). Black dashed lines show isentropic surfaces for θ = 200, 250, … 400 K. (For interpretation of the references to colour in this figure legend, the reader is referred to the web version of this article.)

evolution of the zonal-mean of the mean age at 89°S and 89°N (approximately the latitudes of the most poleward grid points in the model simulations). In both hemispheres, there is seasonality in the magnitude and height of oldest ages within the vertical column at the pole. The annual maximum values (250–300 sols) occur around the equinoxes and minimum values (100–150 sols) around the solstices. In the northern hemisphere (NH) the maximum age in spring is similar to that in autumn, but in the Southern Hemisphere (SH) the spring ages are older than in autumn. (Note, we will use a meteorological, rather than astronomical, definition for seasons, and, e.g., "spring" starts 30° of L_s before the spring equinox and ends 60° of L_s after.) There is also seasonality in the height of the maximum. During the equinoxes the maximum ages in the polar column are located around 70 Pa whereas during winter the maximum is located at a higher altitude (10 Pa in NH and 3 Pa in SH).

The above seasonality in magnitude and altitude of maximum Γ at the poles means that there is large seasonality in the vertical variations of Γ, and hence vertical variations in timescale for transport into polar regions. In autumn and spring there is a rapid increase in Γ with altitude near the surface; the oldest ages occur around 10–100 Pa, and then decrease above 50 Pa. During winter the ages are younger at the surface than at the equinoxes but the peak age occurs at high altitudes (10–1 Pa) and there are weaker vertical gradients. The summer Γ profile differs between the north and south pole: at the north pole the summer vertical gradients below 100 Pa are similar to autumn and spring (Fig. 2**a**), whereas at the south pole there are very weak vertical gradients throughout the atmosphere and no clear maximum in the profile (Fig. 2**b**).

Some of the above seasonality at fixed pressure is related to seasonality in height of isentropic surfaces in polar regions. As the polar atmosphere cools entering winter the isentropes move up in the atmosphere, and the reverse occurs entering summer (red curves in Fig. 2). There is a similar seasonality in the height of near-surface young (c.f. 200 K isentrope) air and the height of the maximum mean age (c.f. 300 K). However, there is still seasonality on isentropic surfaces. This can be seen in Fig. 3**a** which shows the evolution of mean age on the 250 K insentropic surface for northern mid and high latitudes. Similar to what occurs for age on isobaric surfaces between 100 and 50 Pa, the oldest ages at 250 K occur around the equinoxes and youngest around solstice.

The differences between the age in polar regions from that at lower latitudes may be due to the influence of the wintertime polar vortices on tracer transport. To examine this possible connection, we compare the mean age with the potential vorticity (PV) distribution. PV is a commonly used diagnostic of the structure and evolution of the polar vortices (e.g., McIntyre and Palmer, 1983; Waugh et al., 2017), and is defined by

$$\mathrm{PV} = \rho^{-1} \zeta_a \cdot \widetilde{\nabla} \theta$$

where ρ is the fluid density, ζ_a is the absolute vorticity and ∇θ is the gradient of the potential temperature. There are several properties of PV that make it useful for studying polar vortices (e.g., Hoskins et al., 1985): (i) PV is materially conserved for adiabatic, frictionless flows, (ii) other dynamical fields can be determined from PV using "PV inversion", and (iii) PV gradients provide the restoring mechanism for Rossby waves, so that the dynamics and propagation of these waves is best understood by examining the distribution of PV.

Fig. 3b shows the evolution of PV on the 250 K isentropic surface, for northern mid and high latitudes. There is large seasonality in the PV in mid and high latitudes, with low values throughout summer; a rapid increase in values around autumn equinox; maximum values during winter; and then a rapid decline around spring equinox. This larger seasonality in PV is a consequence of the seasonality in the large-scale temperature gradients between low latitudes and the pole, driven by seasonality in solar heating in the polar region. Specifically, PV in the polar region increases in autumn when there is no solar heating in polar regions, and then decays as sunlight returns to the polar regions in spring. The seasonal evolution of PV shown in Fig. 3b highlights the

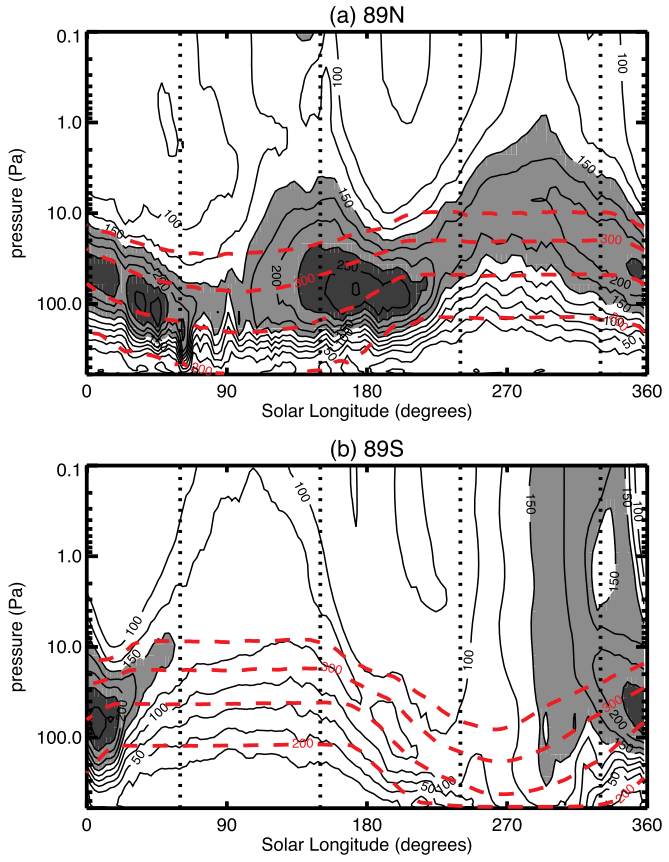

Fig. 2. Pressure-time of zonal-mean Γ at (a) 89°N and (b) 89°S. Contours every 25 sols, with light shading for values larger than 175 sols and dark shading for larger than 225 sols. Red dashed contours show zonal-mean potential temperature (200, 250, 300, 350 K). Vertical dotted lines indicate the boundaries between different, meteorologically defined, seasons (e.g. L_s between 60° and 150° is northern summer). The fields have been smoothed with a 15 sols box-car filter for clarity. (For interpretation of the references to colour in this figure legend, the reader is referred to the web version of this article.)

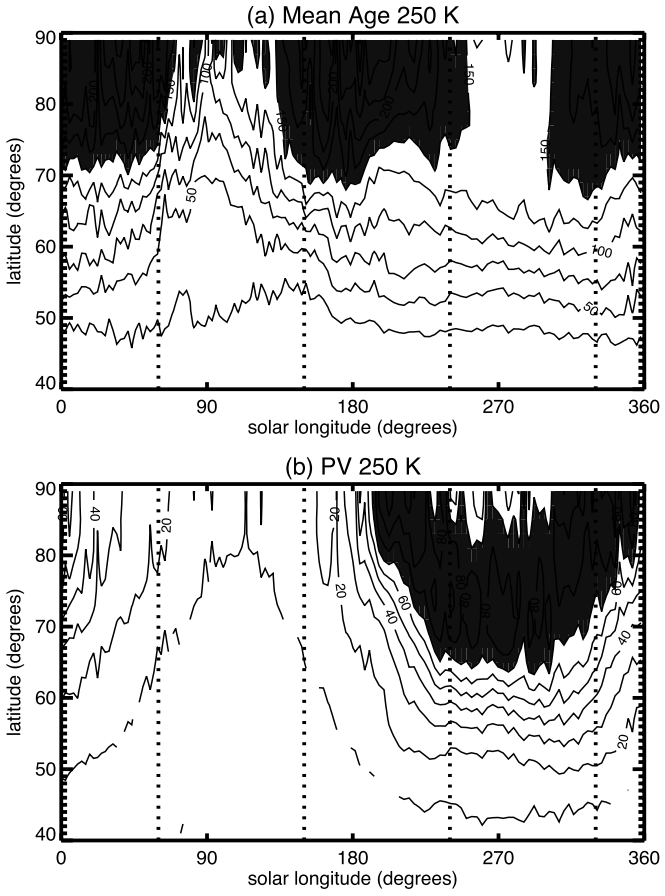

Fig. 3. Latitude-time variation of zonal-mean (a) Γ (contours every 25 sols with shading for values larger than 150 sols) and (b) potential vorticity (PV) (contours every 10×10^{-5} Km^2 kg^{-1} s^{-1} with shading for values larger than 70×10^{-5} Km^2 kg^{-1} s^{-1}) on the 250 K isentropic surface.

formation and decay of the polar vortex, with formation of the polar vortex around the autumn equinox and rapid decay of the vortex around the spring equinox. The decrease in polar PV (and formation of an annular polar vortex) around the winter solstice is due, as discussed in Toigo et al. (2017), to latent heating from the condensation of CO_2.

Comparison of Fig. 3a and 3b show some similarities in the meridional and seasonal variations of mean age and PV: for both fields, there are generally larger values at higher latitudes, and in mid-latitudes (40–60°N) the lowest values occur around summer equinox (L_s = 90°) with roughly constant values from autumn to spring (L_s = 200–360°). But there are differences at high latitudes: The timing of peak values differs between PV and Γ, e.g., for 70–80°N, PV peaks around winter solstice (L_s = 270°) while age peaks around the equinoxes (L_s = 0°, 180°); there is a larger annual cycle in the magnitude of PV than Γ, and although there is a latitudinal minimum in PV at the pole during winter the latitudinal maximum of Γ occurs at the pole.

To explore this further we examine north polar maps of PV and Γ on the 250 K isentropic suface (Fig. 4**)**. These maps clearly show the large seasonality in the magnitude of PV (and hence polar vortex) but weaker seasonality in the magntude of Γ. At summer solstice (L_s = 90°) there is very weak PV through northern mid and high latitudes and no polar vortex; around autumn equinox (L_s = 180°) there is an increase in PV in polar regions; by winter solstice (L_s = 270°) there is an annulus of high PV; and the PV decreases by the time of spring equinox (L_s = 0°). There is also seasonality in magnitude of the age, but the amplitude of seasonal variation is smaller (area with Γ > 150 sols for each time shown) and the timing of the annual maximum values differs from PV (largest values occur around both L_s = 180° and 360°). Note that the centroids of the regions with large Γ are typically offset from the pole, and thus the zonal averaging applied in Figs. 1–3 will tend to smooth over these larger local values.

The differences in the seasonality of PV and Γ are due primarily to the differing impact of diabactic processes on the two fields. As discussed above, the large seasonality in PV is a consequence of the seasonality in diabatic heating and cooling, and resulting large-scale temperature gradient. This seasonality of diabatic heating and cooling does not directly impact Γ, as its source is constant in space and time, and the seasonality of Γ is instead driven by transport processes.

Although the seasonality of the magnitude varies, the shape of PV and Γ contours in Fig. 4 are very similar for all seasons. (There is a small region of high Γ at L_s = 90° that does not appear in the PV, but the shape of the larger region with high Γ is similar to shape of the PV contours.) This agreement between PV and Γ is consistent with a large body of literature for Earth's stratospheric polar vortices that have shown weak transport across PV contours, especially across strong PV gradients, and that have shown similar shapes for contours of PV and chemical or idealized tracers (e.g., Leovy et al., 1985; Waugh et al., 1994). It is also consistent with the close relationship between PV and ozone in the Martian atmosphere (Holmes et al., 2017). It therefore appears that the polar vortex and PV structure can explain much of the sub-seasonal evolution of Γ in high latitudes.

While the PV structure can explain much of the sub-seasonal evolution of Γ, there are differences in evolution around L_s = 230° − 250°. During this period, an annular polar vortex forms and there is a

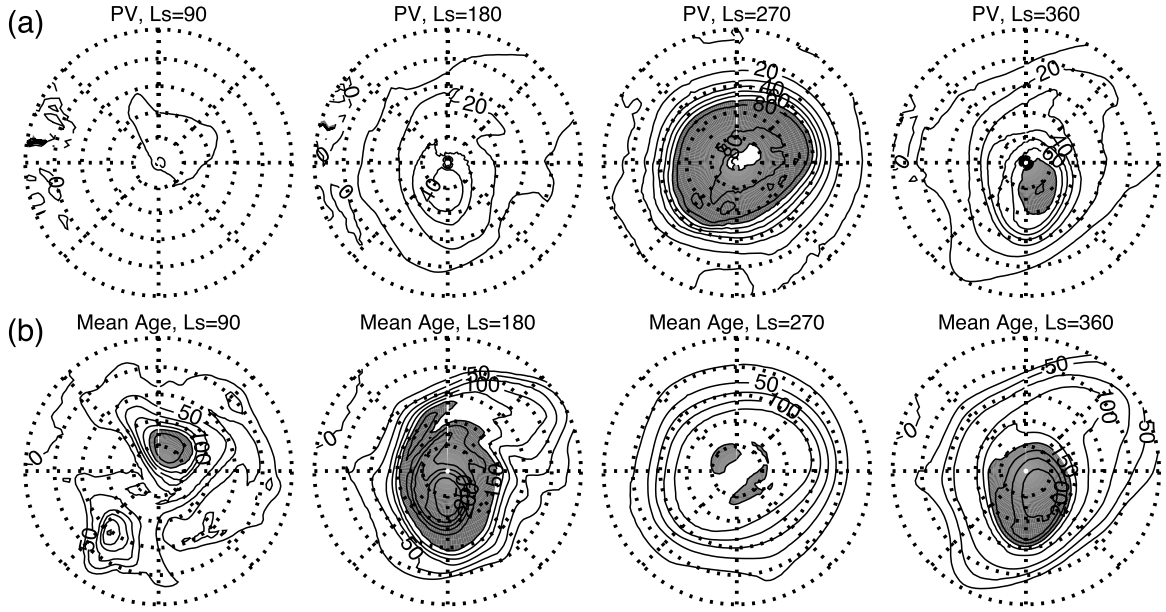

Fig. 4. North polar stereographic projection maps of (a, upper) PV and (b, lower) mean age on the 250 K isentropic at the equinoxes and solstices. The outer latitude is 40°N and 0° longitude is at the bottom of the maps. PV contours every 10×10^{-5} Km^2 kg^{-1} s^{-1}, with shading for PV $> 70 \times 10^{-5}$ Km^2 kg^{-1} s^{-1}. Mean age contours every 25 sols, with shading for values larger than 150 sols.

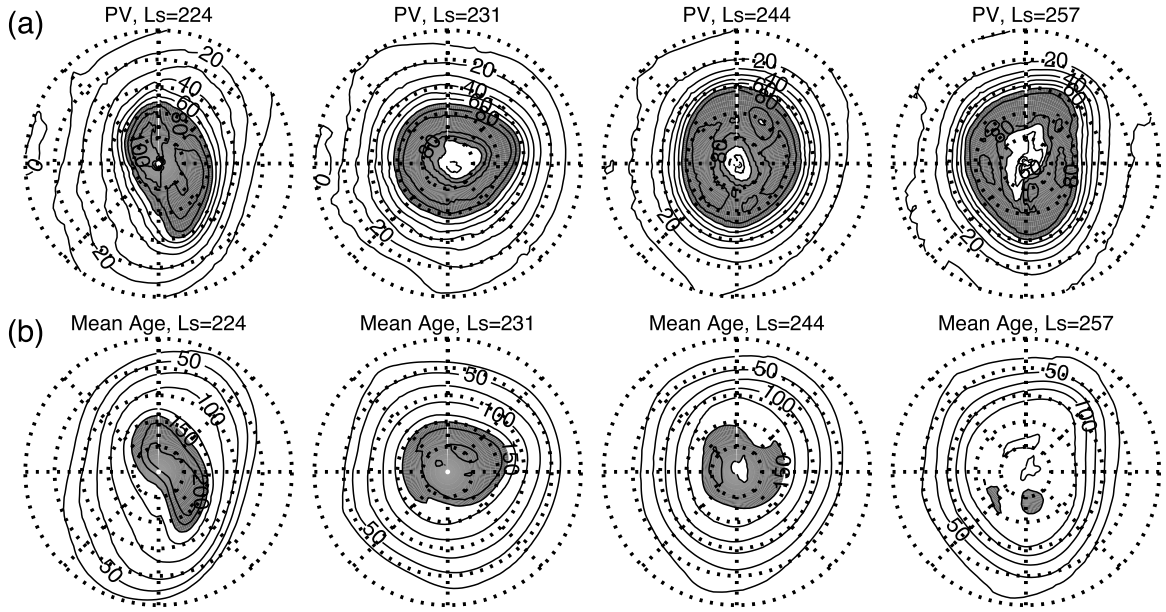

Fig. 5. As in Figure 4 except for maps at $L_s = 224°$ to 257°.

decrease in polar Γ (Fig. 3). As shown in Fig. 5, at $L_s = 224°$ there is a monopolar PV distribution but by $L_s = 231°$ an annular PV structure has formed, and although the shape varies with time there is an annular structure with similar maximum PV for the rest of the period shown (and until $L_s = 300°$). There is again a good correspondence between the shape of Γ and PV contours, but there is no annular structure in the Γ field and the maximum magnitude of Γ decreases through the period shown.

The decrease in polar Γ is consistent with increased mixing of air between the interior and exterior of the annular vortex. A Mars-like annular vortex will, in the absence of a strong restoring force or mechanism, break up into smaller vortices that coalesce into a monopolar vortex. However, when there is a restoring force (e.g., radiative processes) any smaller vortices that form do not coalesce together and the vortex remains annular (Seviour et al., 2017). Toigo et al. (2017) and Seviour et al. (2017) hypothesized that the tendency for the annulus to form multiple smaller-scale vortices on short timescales may allow for enhanced cross-jet transport of tracers across the high PV region of the Martian annular polar vortex. Such enhanced cross-jet transport would then lead to a decrease in Γ within the vortex, as younger mid-latitude air "leaks" into the vortex core via the regions of relatively weaker PV gradients between these smaller-scale vortices.

The evolution of Γ during the autumn-winter transition varies with altitude. As shown in Fig. 2 the timing and magnitude of decrease in Γ varies with height (or isentropic surface), with earlier and larger decrease for lower levels. These differences are illustrated in Fig. 6 which shows maps of Γ on the (a) 300 K and (b) 200 K isentropic surfaces for this transition period. At the 200 K level there is a small region with old ages, and the peak ages decrease from about 180 to 80 sols between $L_s = 210°$ and 230°. In contrast, at the 300 K level there is a

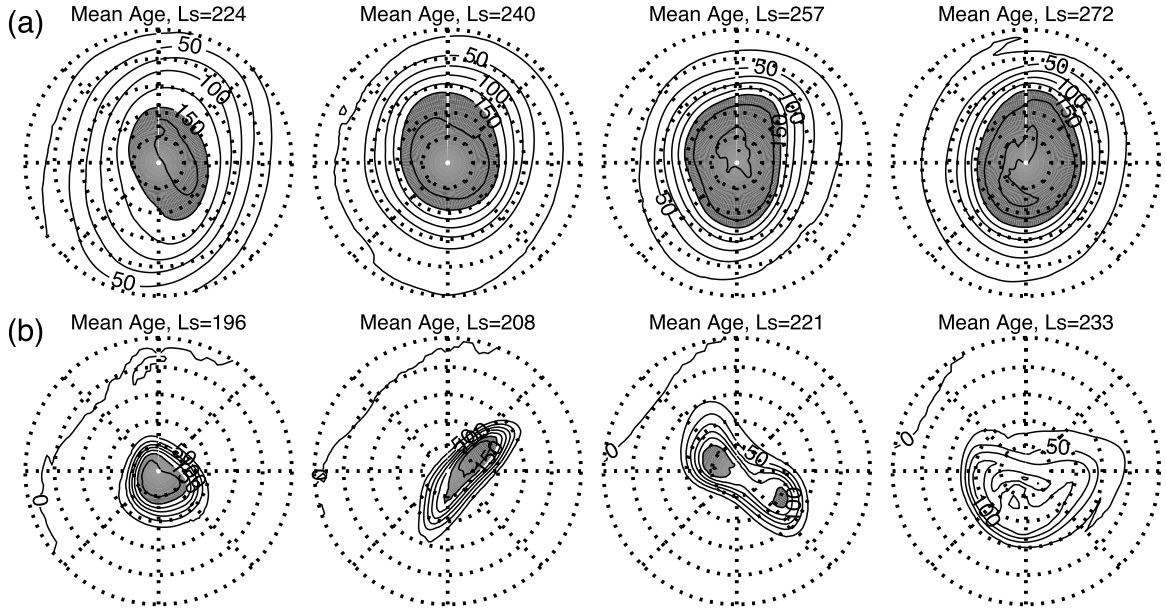

Fig. 6. As in Figure 4(b) except for maps of mean age on (a, upper) 300 and (b, lower) 200 K isentropic surfaces.

larger region of older ages and the peak values are above 160 sols through the period shown and throughout winter. These differences in Γ between levels are consistent with the differences in the polar vortex structure. The polar vortex is much smaller and more disturbed at the 200 K level than it is at the 300 K level, and as a result there is more mixing of younger air into the polar regions at lower altitudes.

The above discussion has focused on the northern polar region, but there is a similar evolution in southern high latitudes. In particular, during autumn there is a transition from a monopolar to annular PV structure and during this period there is decrease in Γ in polar regions (Fig. 7). This is, again, consistent with increased mixing between the interior and exterior of the polar vortex when it has a zonal-mean annular PV structure (with multiple smaller-scale vortices).

Finally, we consider the transport into polar regions near the surface. In this region, there is not a strong or coherent polar vortex (as defined by the magnitude and shape of the PV contours in this region; not shown), and numerous observational and modeling studies have shown that near-surface baroclinic instability and transient waves are common near the surface (e.g., Barnes, 1980; Barnes et al., 1993; Wilson et al., 2002; Banfield et al., 2004). As discussed above, the seasonality of transport near the surface also differs from higher altitudes, with youngest polar Γ occurring during winter and oldest during summer. Mixing associated with the transient waves is a possible cause of this seasonality, with stronger poleward eddy fluxes in autumn/winter transporting more young air from the source region and decreasing the mean age of polar air during winter. However, there is a minimum in near-surface transient eddy activity around the winter solstice (the so-called "solsticial pause") (e.g., Wang et al., 2013, Lewis et al., 2016), which is inconsistent with the required increase in poleward transport during winter. This suggests that transport by the mean flow may be responsible for this pattern of seasonality. There is in fact large seasonal variation in near-surface mean meridional flow in mid to high latitudes, with poleward flow in autumn-winter but equatorial flow in spring-summer (in both seasons this region is poleward of the

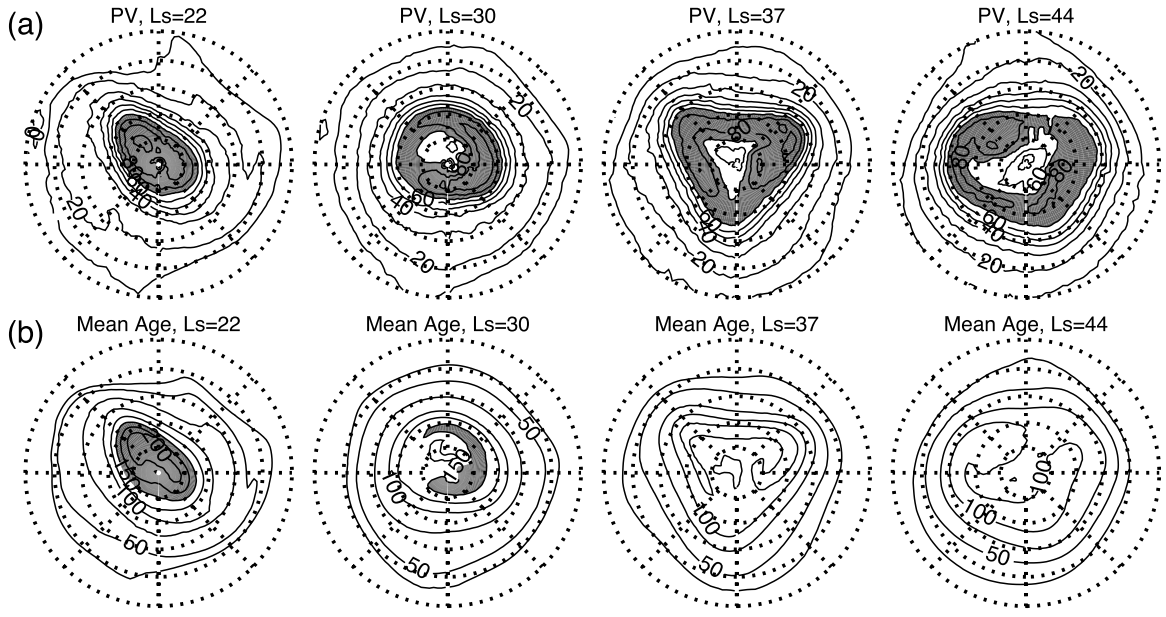

Fig. 7. As in Fig. 4 except for southern hemisphere and L_s = 22° to 44°. Outer latitude is 40°S, and absolute value of PV shown.

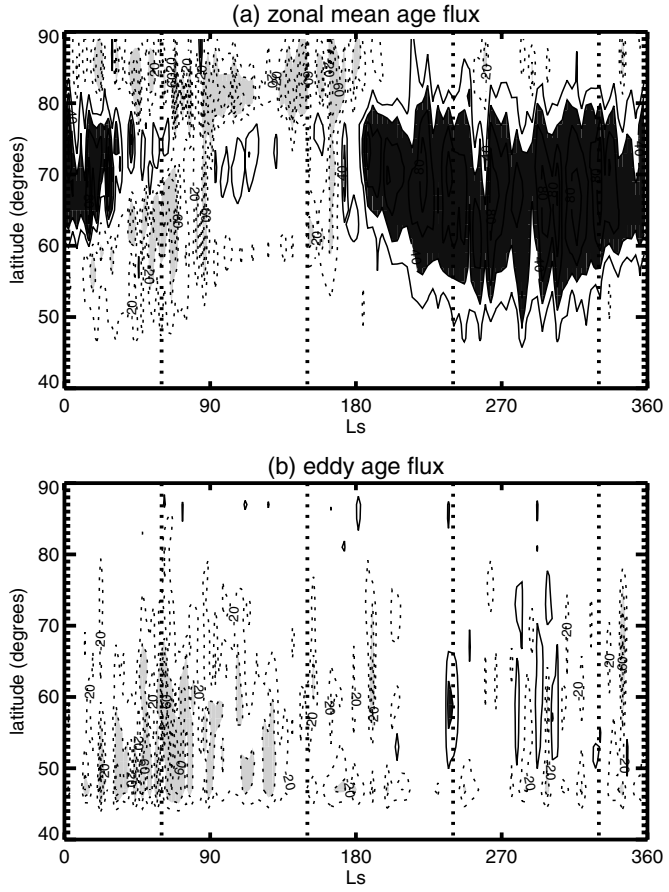

Fig. 8. Latitude-time variation of (a) zonal-mean meridional age flux and (b) eddy meridional age flux on the 566 Pa surface. Contours every 20 sol m s^{-1} with dark gray shading for values larger than 60 and light gray shading for values less than −60 (zero contour not shown).

large Hadley cell, and instead influenced by the reverse "Ferrell" cells). This seasonality is consistent with variations in polar age, with the autumn-winter poleward flow transporting young air into polar regions but spring-summer equatorial flow opposing such transport. Furthermore, analysis of meridional age fluxes in our simulations shows that the mean age flux ($\bar{v}\ \bar{\Gamma}$, where $\bar{v}$ is the zonal mean meridional velocity) is generally much larger than the eddy age flux ($\overline{v'\Gamma'}$, where v' is the deviation from the zonal mean), see Fig. 8. Thus it appears that seasonality in the transport by the near-surface zonal mean flow is main cause of the youngest near-surface polar ages in winter. This is consistent with the analysis of Lian et al. (2012) showing the importance of mean meridional fluxes for transporting argon into the polar regions.

4. Sensitivity simulations

As described in Section 2, we also performed several additional simulations to examine the sensitivity of the age distribution to CO_2 microphysics, dust loading, and size of the surface source region.

4.1. No CO2 microphysics

As discussed in Toigo et al. (2017), when the CO_2 microphysics parameterization is disabled in a "no-CO_2-latent-heating" simulation, there is no longer an annular PV structure during winter. Instead, there remains a monopolar PV distribution, with peak PV values much larger than in the standard (CO_2 phase changes enabled) simulation (Fig. 9, but also see Figs. 1–3 of Toigo et al. (2017)). To examine what impact this has on the transport we included the mean age tracer in the "no-CO_2-latent-heating" simulation. The global distribution of Γ in the "no-CO_2-latent-heating" simulation is very similar to that in the standard simulation shown above, with similar seasonality and consistency with the mean meridional circulation. There are, however, significant differences in the polar lower atmosphere. In particular, in the "no-CO_2-latent-heating" simulation large values of Γ are maintained from autumn to spring, see Fig. 9. This maintenance of old Γ in polar region through the winter also occurs in the southern hemisphere (not shown).

The fact that there is a monopolar PV structure and maintenance of a polar region with old Γ in the "no-CO_2-latent-heating" simulation supports the hypothesis and analysis above suggesting that the decrease in polar Γ in the standard simulation is due to there being an annular vortex which has less of a transport barrier than a monopolar vortex.

Note, to test if the removal of CO_2 (by condensation in the polar night) is contributing to the decrease in age, rather than transport across the annular vortex edge, an additional simulation was performed where the effect of latent heating due to CO_2 condensation and sublimation was enabled (i.e., air temperatures could increase or decrease), but the removal or addition of CO_2 in the air column after this energy exchange was disabled. This simulation still produces an annular PV structure, as it is the latent heating and not the removal of CO_2 itself that matters for the formation of an annulus (Toigo et al., 2017), and there is also still a decrease of Γ in polar regions during this period. Thus, it is the annular PV structure and not removal of CO_2 that is also important for the decrease of age during this period.

4.2. Additional dust loading

Previous studies have shown that increasing the dust loading (e.g., as a proxy for the presence of a global or large regional dust storm) leads to a stronger mean meridional circulation, as well as a mid-winter transient warming in the northern polar region (e.g., Wilson, 1997, Guzewich et al., 2016). To examine what impact this increase in meridional circulation has on tracer transport we include the mean age tracer in an "additional dust" simulation with twice the dust opacity of the standard simulation during northern winter (see Section 2).

The age distributions at the equinoxes and northern summer are virtually the same as the standard simulation (as the dust loading is the same during these periods), but at northern winter solstice there are much younger ages in low-mid latitudes in the additional dust simulation (Fig. 10a), e.g., Γ at the equator and 1 Pa is about 90 sols in the "standard simulation" but only about 40 sols in the "additional dust" simulation. This younger Γ in the "additional dust" simulation is consistent with a stronger mean meridional circulation in this simulation (red contours in Fig. 10a; see also Guzewich et al. (2016)).

There are also differences in the northern polar region (Fig. 10). There is a stronger polar jet that is nearer the pole in the additional dust simulation, and this results in a more confined region of old Γ that extends to higher altitudes. Furthermore, as discussed in Guzewich et al. (2016) and Toigo et al. (2017), there is a transient vortex warming near the winter solstice in the "additional dust" simulation in which the temperatures increase, CO_2 condensation essentially halts and there is no latent heating, and the annular vortex rapidly collapses into a small monopolar vortex. At the end of the transient vortex warming, polar temperatures again drop below CO_2 condensation temperatures and an annular vortex reforms (see Fig. 4a of Toigo et al. (2017)). There is similar evolution of Γ at this period, with the region of oldest Γ values shrinking to a small circular region over the pole during the transient warming (not shown).

4.3. Height and width of source region

In the above simulations, the source region (i.e., the region where the air is assigned an age of 0) is from the surface to 10 km between 45°S and 45°N. To test the sensitivity of the age distribution to these choices we performed additional simulations with either a shallower

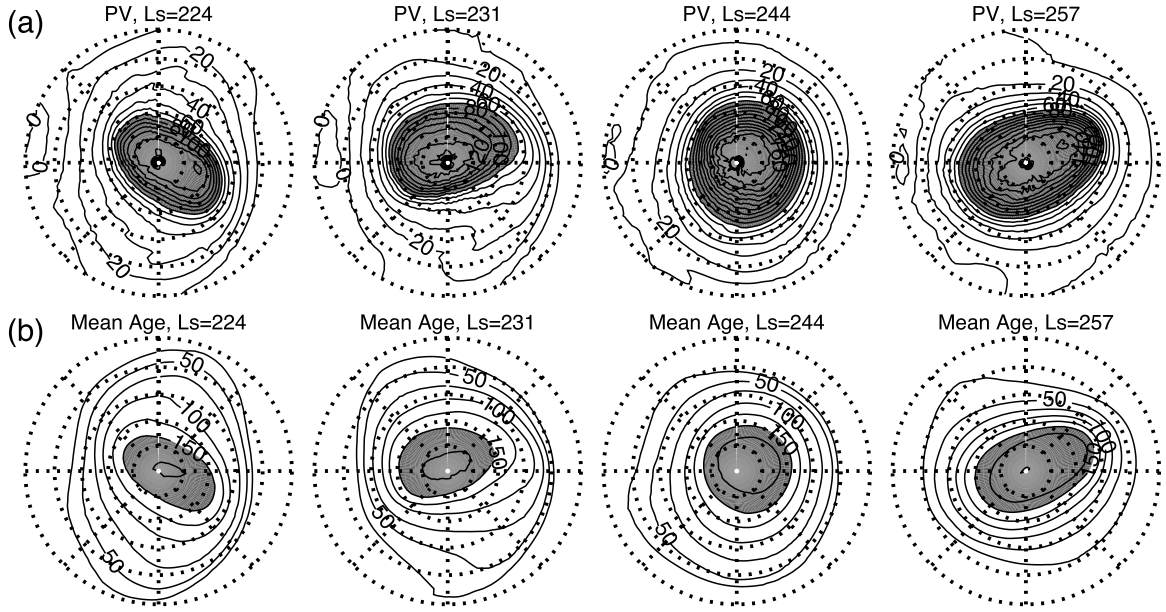

Fig. 9. As in Fig. 4 except for "no-CO_2-latent-heating" simulation and L_s = 209° to 304°.

depth ("shallow source" simulation, with a source region from the surface to only 5 km but still between 45°S and 45°N) or a narrower width ("narrow source" simulation with a source region from the surface to 10 km but only between 30°S to 30°N). The Γ distributions in both these simulations are very similar to those in the standard simulation, with the differences from the standard simulation being smaller than the interannual variation in the multi-year standard simulation (not shown). This indicates limited sensitivity to depth or width of source region, and that the above conclusions for the standard (and other sensitivity) simulations will hold for shallower or narrower source regions.

5. Conclusions

Simulations of an idealized tracer within the MarsWRF general circulation model indicate that the mean time since air in the Martian atmosphere was in the low-to-mid-latitude boundary layer (the so-called "mean age")

- is less than 100 sols for most of the atmosphere;
- is oldest in the polar lower atmosphere (10–100 Pa), where it can exceed 300 sols;
- has substantial vertical and seasonal variations in polar regions.

The spatial and seasonal variations of the mean age in low- and mid-latitudes are closely connected to the Hadley cell circulations, whereas at high-latitudes, variations in mean age are connected with the evolution of the polar vortices. The oldest ages occur in the polar lower atmosphere around the equinoxes, and the age decreases during the autumn to winter transition. This autumn-winter decrease occurs because of mixing of polar and mid-latitude air when the polar vortex is an annulus of high PV. There is no autumn-winter decrease in age in simulations with CO_2 phase changes disabled, and thus no latent heating, where only a monopolar vortex forms.

As mentioned in Section 1, there have been few previous studies of the tracer transport in Mars atmosphere. One exception is Barnes et al. (1996), who calculated a "ventilation" time scale for air above 100 Pa, defined as the mass in the region above 100 Pa divided by mass flux into this region. Their simulations show a ventilation time of approximately 60 sols for solstice conditions and approximately 180 sols for equinox conditions. The faster transport during solstice compared to equinox is consistent with the mean age calculated here, but the mean age is much younger than the Barnes et al. ventilation time (i.e., low latitude mean age at 100 Pa is only 10–20 sols). It is not clear how much of this difference is because the two transport times are measuring different aspects of the transport or due to differences in the models. The model used in Barnes et al. (1996) had much lower

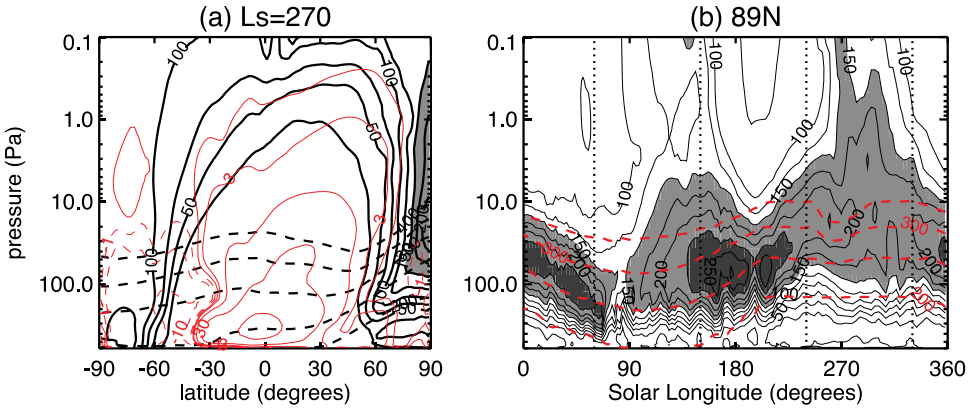

Fig. 10. (a) As in Fig. 1d except for the "additional dust" simulation, and (b) as in Fig. 2a except for the "additional dust" simulation. (For interpretation of the references to colour in the text legend, the reader is referred to the web version of this article.)

horizontal and vertical resolution than the MarsWRF simulations presented here (7.5° latitude × 9° longitude spatial resolution and 13 vertical levels compared to 2° × 2° spatial resolution and 52 vertical levels in our MarsWRF simulations), and previous studies have shown that the mean-meridional and polar circulations are sensitive to model resolution (e.g., Toigo et al., 2012). It would therefore be useful (important) to repeat the type of ideal age simulations presented here with another Martian general circulation model and to also test the sensitivity to the transport scheme used (e.g., as in Lian et al. (2012) for argon simulation).

While there are few previous studies of the time scales of transport in the Martian atmosphere, there is a large body of literature examining the age of air in Earth's atmosphere. The majority of these studies have focused on the stratosphere, and have shown that the mean age is around 3–5 years through most the stratosphere with the oldest air in the upper stratosphere (e.g., Waugh and Hall (2002) and references therein). These ages are much older than in our MarsWRF simulations, none of which even exceed half a (Martian) year. However, as discussed in Waugh et al. (2016) with respect to polar vortices, it is more appropriate to compare transport in the Martian atmosphere with that in Earth's troposphere. The mean time since tropospheric air has been at the surface is much less than in the stratosphere, with mean ages generally less than 100 days for a global surface source region (Krol et al., 2017) and generally comparable with the mean ages presented here.

This study has considered a very idealized tracer and it is not possible to directly compare with observed constituents in the Martian atmosphere. However, variations in the simulated mean age may be useful for understanding distributions of dust, water vapor and other trace gases. In particular, the variations in the mean age in polar regions suggest that the transport of dust into polar regions and the mixing of polar air (with, e.g., low water vapor and high ozone concentrations) into mid-latitudes varies with altitude as well as season. For example, Guzewich et al. (2015) found a 20–40° of solar longitude lag between observed dust storms and a global opacity response. This timescale is comparable to the global low-altitude mean air ages we see in all seasons, suggesting that dust lifted by local and regional storms in the low and mid-latitudes can be transported globally in short periods. Focusing specifically on the polar atmosphere, observations have shown that the air inside the winter polar vortices is nearly devoid of dust (Guzewich et al., 2016; Montabone et al., 2015), while our simulations suggest that the near-surface polar region mixes with the (typically) dusty low-latitude air on short (< 20 sols) timescales. This suggests that dust should be constantly entering the lower winter polar atmosphere and hence the lack of observable dust implies rapid microphysical processes (e.g., scavenging by water or CO_2 ice particles) occur.

Acknowledgements

The authors gratefully recognize funding from the NASA Mars Fundamental Research Program through grant NNX14AG53G. Simulations were performed on the supercomputers of the NASA Advanced Supercomputing Division at the NASA Ames Research Center.

Supplementary materials

Supplementary material associated with this article can be found, in the online version, at doi:10.1016/j.icarus.2018.08.002.

References

Banfield, D., et al., 2004. Traveling waves in the Martian atmosphere from MGS TES nadir data. Icarus 170, 365–403.
Barnes, J.R., 1980. Time spectral analysis of mid-latitude disturbances in the Martian atmosphere. J. Atmos. Sci. 37, 2002–2015.
Barnes, J.R., et al., 1993. Mars atmospheric dynamics as simulated by the NASA/ Ames general circulation model. 2. Transient baroclinic eddies. J. Geophys. Res. 98, 3125–3148.
Barnes, J.R., Walsh, T.D., Murphy, J.R., 1996. Transport timescales in the Martian atmosphere: General circulation model simulations. J. Geophys. Res. 101, 16881–16889.
Bertaux, J.-L., et al., 2005. Nightglow in the upper atmosphere of Mars and implications for atmospheric transport. Science 307, 566–569.
Clancy, R.T., Grossman, A.W., Wolff, M.J., James, P.B., Rudy, D.J., Billawala, Y.N., Sandor, B.J., Lee, S.W., Muhleman, D.O., 1996. Water vapor saturation at low altitudes around Mars aphelion: a key to Mars climate? Icarus 122, 36–62.
Guzewich, S.D., Toigo, A.D., Waugh, D.W., 2016. The effect of dust on the Mars Polar vortices. Icarus 278, 100–118.
Guzewich, S.D., Toigo, A.D., Kulowski, L., Wang, H., 2015. Mars Orbiter Camera climatology of textured dust storms. Icarus 258, 1–13.
Haine, T.W., Hall, T.M., 2002. A generalized transport theory: water-mass composition and age. J. Phys. Oceanogr. 32, 1932–1946.
Hall, T.M., Plumb, R.A., 1994. Age as a diagnostic of stratospheric transport. J. Geophys. Res. 99, 1059–1070.
Holmes, J.A., Lewis, S.R., Patel, M.R., 2017. On the link between Martian total ozone and potential vorticity. Icarus 282, 104–117.
Hoskins, B.J., McIntyre, M.E., Robertson, A.W., 1985. On the use and significance of isentropic potential vorticity maps. Q. J. R. Meteorol. Soc. 111, 877–946.
Krol, M., et al., 2017. Age of Air as a diagnostic for transport time-scales in global models. Geosci. Model Dev. Discuss. https://doi.org/10.5194/gmd-2017-262.
Leovy, C.B., et al., 1985. Transport of Ozone in the middle stratosphere: evidence for planetary wave breaking. J. Atmos. Sci. 42, 230–244.
Lewis, S.R., Mulholland, D.P., Read, P.L., Montabone, L., Wilson, R.J., Smith, M.D., 2016. The solsticial pause on Mars: 1. A planetary wave reanalysis. Icarus 264, 456–464.
Lewis, S.R., Collins, M., Read, P.L., Forget, F., Hourdin, F., Fournier, R., Hourdin, C., Talagrand, O., Huot, J.P., 1999. A climate database for Mars. J. Geophys. Res. 104, 24177–24194.
Lian, Y., Richardson, M.I., Newman, C.E., Lee, C., Toigo, A.D., Mischna, M.A., Campin, J.M., 2012. The Ashima/MIT Mars GCM and argon in the Martian atmosphere. Icarus 218 (2), 1043–1070.
Montabone, L., Forget, F., Millour, E., Wilson, R.J., Lewis, S.R., Kass, D., Kleinböhl, A., Lemmon, M.T., Smith, M.D., Wolff, M.J., 2015. Eight-year climatology of dust optical depth on Mars. Icarus. http://doi.dx.doi.org/10.1016/j.icarus.2014.12.034.
Montmessin, F., Forget, F., Rannou, P., Cabane, M., Haberle, R.M., 2004. Origin and role of water ice clouds in the Martian water cycle as inferred from a general circulation model. J. Geophys. Res. 109 (E10).
Montmessin, F., Lefèvre, F., 2013. Transport-driven formation of a polar ozone layer on Mars. Nat. Geosci. 6, 930–933.
Newman, C.E., Lewis, S.R., Read, P.L., Forget, F., 2002. Modeling the Martian dust cycle, 1, representations of dust transport processes. J. Geophys. Res. 107, 5123.
Orbe, C, Holzer, M, Polvani, LM, Waugh, DW, 2013. Air-mass origin as a diagnostic of climate change in tropospheric transport. J. Geophys. Res. 118, 1459–1470.
Orbe, C., et al., 2017. Large-scale tropospheric transport in the Chemistry Climate Model Initiative (CCMI) simulations. Atmos. Chem. Phys. Discuss. https://doi.org/10.5194/acp-2017-1038.
McIntyre, M.E., Palmer, T.N., 1983. Breaking planetary waves in the stratosphere. Nature 305, 593–600.
Plumb, R.A., Mahlman, J.D., 1987. The zonally averaged transport characteristics of the GFDL general circulation/transport model. J. Atmos. Sci. 44 (2), 298–327.
Richardson, M.I., Toigo, A.D., Newman, C.E., 2007. PlanetWRF: a general purpose, local to global numerical model for planetary atmospheric and climate dynamics. J. Geophys. Res. 112, E09001. https://doi.org/10.1029/ 2006JE002825.
Seviour, W.J., Waugh, D.W., Scott, R.K., 2017. The Stability of Mars's Annular Polar Vortex. J. Atmos. Sci. 74, 1533–1547.
Skamarock, W.C., Klemp, J.B., 2008. A time-split nonhydrostatic atmospheric model for weather research and forecasting applications. J. Comput. Phys. 227, 3465–3485.
Skamarock, W.C., Klemp, J.B., Dudhia, J., Gill, D.O., Barker, D., Duda, M.G., Huang, X., Wang, W., Powers, J.G., 2008. A Description of the Advanced Research WRF Version 3. NCAR Technical Note NCAR/TN-475+STR. Natl. Cent. for Atmos. Res., Boulder, CO. https://doi.org/10.5065/D68S4MVH.
Smith, M.D., 2002a. Interannual variability in TES atmospheric observations of Mars during 1999-2003. Icarus 167 (1), 148–165. https://doi.org/10.1016/j.icarus.2003.09.010.
Smith, M.D., 2002b. The annual cycle of water vapor on Mars as observed by the thermal emission spectrometer. J. Geophys. Res. 107 (E11).
Sprague, A.L., Boynton, W.V., Kerry, K.E., Janes, D.M., Kelly, N.J., Crombie, M.K., Nelli, S.M., Murphy, J.R., Reedy, R.C., Metzger, A.E., 2007. Mars' atmospheric argon: tracer for understanding Martian atmospheric circulation and dynamics. J. Geophys. Res. 112 (E3).
Toigo, A., Lee, C., Newman, C.E., Richardson, M.I., 2012. The impact of resolution on the dynamics of the Martian global atmosphere: Varying resolution studies with the MarsWRF GCM. Icarus 221, 276–288.
Toigo, A.D., Waugh, D.W., Guzewich, S.D., 2017. What causes Mars' annular polar vortices? Geophys. Res. Lett. 44, 71–78.
Wang, H., Richardson, M.I., Toigo, A.D., Newman, C.E., 2013. Zonal wavenum- ber three traveling waves in the Northern Hemisphere of Mars simulated with a general circulation model. Icarus 223, 654–676.
Waugh, D.W., Hall, T.M., 2002. Age of stratospheric air: theory, observations, and models. Rev. Geophys. 40 (4). https://doi.org/10.1029/2000RG000101.
Waugh, D.W., et al., 1994. Transport of material out of the stratospheric Arctic vortex by Rossby wave breaking. J. Geophys. Res. 99, 1071–1088.

Waugh, D.W., et al., 2013. Tropospheric SF6: Age of air from the Northern Hemisphere mid-latitude surface. J. Geophys. Res. 118, 11429–11441.
Waugh, D.W., Sobel, A., Polvani, L.M., 2017. What is the polar vortex and how does it influence weather. Bull. Am. Meteorol. Soc. 98, 37–44.
Waugh, D.W., Toigo, A.D., Guzewich, S.D, Greybush, S.J., Wilson, R.J., Montabone, L., 2016. Martian Polar vortices: comparison of reanalyses. J Geophys. Res. 121. https://doi.org/10.1002/2016JE005093.
Wilson, R.J., et al., 2002. Traveling waves in the northern hemisphere of Mars. Geophys. Res. Lett. 29 (14). https://doi.org/10.1029/2002GL01486.
Wilson, R.J., et al., 1997. A general circulation model simulation of the Martian polar warming. Geophys. Res. Lett. 24 (2), 123–126.